Strong to ultrastrong coherent coupling measurements in a YIG/cavity system at room temperature

Guillaume Bourcin [1,2,*] Jeremy Bourhill,[3] Vincent Vlaminck [1,2] and Vincent Castel [1,2,†]

[1]*IMT Atlantique, Technopole Brest-Iroise, CS 83818, 29238 Brest Cedex 3, France*

[2]*Lab-STICC (UMR 6285), CNRS, Technopole Brest-Iroise, CS 83818, 29238 Brest Cedex 3, France*

[3]*Quantum Technologies and Dark Matter Labs, Department of Physics, University of Western Australia, 35 Stirling Highway, 6009 Crawley, Western Australia*

We present an experimental study of the strong to ultrastrong coupling regimes at room temperature in frequency-reconfigurable three-dimensional reentrant cavities coupled with a yttrium-iron-garnet slab. The observed coupling rate, defined as the ratio of the coupling strength to the cavity frequency of interest, ranges from 12% to 59%. We show that certain considerations must be taken into account when analyzing the polaritonic branches of a cavity spintronic device where the rf field is highly focused in the magnetic material. Our observations are in excellent agreement with electromagnetic finite-element simulations in the frequency domain.

I. INTRODUCTION

Cavity spintronics is an emerging research field that investigates light-matter interactions within magnetism, specifically the interactions between cavity photons and the quanta of spin waves based on the magnetic dipole interaction—magnons. At the core of cavity spintronics are cavity-magnon polaritons (CMPs), which are the associated bosonic quasiparticles, i.e., hybridized cavity-magnon-photon states in the strong-coupling regime. Cavity spintronics has drawn growing interest since the first theoretical prediction in 2010 [1], and then shortly after experimental demonstration of CMPs at both millikelvin (mK) temperatures [2,3] and room temperature (RT) [4]. Cavity spintronics display a broad range of applicability for quantum information systems and rf devices, such as adjustable sensitive filters [5–7], isolators or circulators [8], gradient memories [9] and for engineering chiral states of electromagnetic radiation [10,11].

In a cavity–magnon system, when the magnon frequency is tuned by an externally applied static magnetic field towards the cavity resonance frequency, the system undergoes hybridization (e.g., forms a CMP) with a characteristic anticrossing signature in the dispersion spectrum. The interaction is quantified by the coupling strength $g/2\pi$ and by its ratio g/ω with the cavity frequency $\omega/2\pi$. When the coupling $g/2\pi$ is larger than the system's losses, there exist three different coupling regimes. These have commonly been referred to as: (i) strong coupling when $g/\omega < 0.1$, (ii) ultrastrong coupling (USC) for $0.1 < g/\omega < 1$, and (iii) deep-strong coupling (DSC) for $g/\omega > 1$, a regime that still remains largely unexplored. The value of $g/\omega = 0.1$ is considered as a threshold between the SC and USC regimes, but this is only a historical convention, supposedly indicating the cutoff beyond which the coupling rate g represents a "sizeable fraction" of the system energy and therefore cannot be deemed to be a slowly rotating term in the rotating-wave approximation.

The USC regime was predicted theoretically in intersubband cavity polaritons in 2005 [12] and first observed in 2009 [13] in n-doped GaAs quantum wells embedded in a microcavity, with $g/\omega = 0.11$. Since this experimental observation, several research groups have experimentally achieved the USC regime [14,15] in different systems such as superconducting circuits [16], polaritons [17], and optomechanics [18]. So far, the USC regime in cavity spintronics has been experimentally achieved at low [19–23] and room [24,25] temperatures, and investigated theoretically [26,27].

Very recently, Golovchanskiy *et al.* [23] proposed an approach to achieve on-chip USC hybrid magnonic systems reaching $g/\omega = 0.6$ and based on superconducting/insulating/ferromagnetic multilayered microstructures operating below 10 K. They highlighted in particular the drastic failure of currently adopted models in the USC regime.

Here, we present measurements and simulations of a reconfigurable hybrid system that allows the study of the transition from the SC to USC regimes at room temperature in the 0.1–15 GHz frequency range. We utilize a magnetic field-focusing double-post reentrant cavity first described by Goryachev *et al.* [19]. A set of three different resonators (by their dimensions and post shapes) allow us to follow the evolution of the coupling strength through USC regime (starting from the SC/USC limit). With these results we confirm that it is necessary to add an extra term in the expression of the ferromagnetic resonance (FMR) frequency equation to accurately describe the observed hybridization (measurements and simulations) with the commonly used Dicke model [28]. We show that this additional term does not depend on the coupling rate but on the level of confinement of the rf magnetic field in the magnetic material. Moreover, this added term can be negligible in the SC regime, while it is essential in the USC regime.

---

*guillaume.bourcin@imt-atlantique.fr
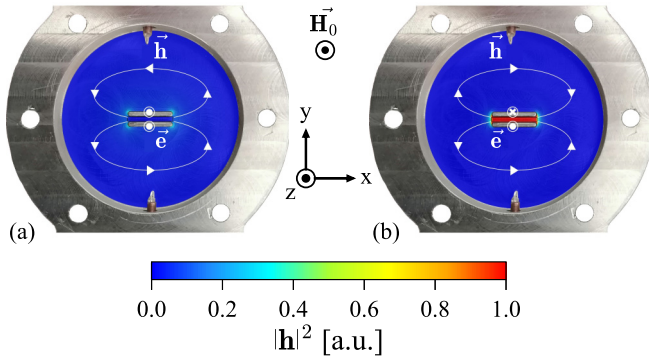
†vincent.castel@imt-atlantique.fr

FIG. 1. Reentrant cavity with electromagnetic simulation overlay where $|\mathbf{h}|^2$ is displayed for the first two photonic modes: (a) the DM and (b) the BM.

II. HYBRID SYSTEM DESCRIPTION

The hybrid system presented here is made of a commercial single crystal of YIG (yttrium iron garnet, $Y_3Fe_5O_{12}$) and a modified reentrant cavity. The YIG is a slab of $3.82 \times 6.09 \times 0.61$ mm^3.

The multiple post reentrant cavity [19] is a unique type of microwave cavity. There are two first-order resonant modes, termed the dark mode (DM) and the bright mode (BM). Both contain the electric field of the mode between the top of the post and the lid of the cavity. For the DM [as shown in Fig. 1(a)], the rf electric fields (**e**-fields) focused above the two posts are in phase, resulting in the circulating rf magnetic fields (**h**-fields) destructively interfering in the region between the posts (hence "dark"), while the opposite is true for the BM [as shown in Fig. 1(b)]. The advantages of such a cavity are threefold: First, the highly localized electric field results in extremely large frequency sensitivity to any perturbations inside this region (displacement of the containment area or modification of the dielectric material). Second, the physical separation of the electric and magnetic fields permits separate interaction with both magnetic and electrically sensitive devices at different locations, potentially simultaneously. Finally, the magnetic field focusing between the posts results in extremely strong interactions with any magnetically susceptible material placed there.

The interaction between a single-cavity mode and the FMR can be described by two coupled harmonic oscillators, for which the Hamiltonian is read as

$$\hat{H} = \hat{H}_c + \hat{H}_m + \hat{H}_{\text{int}}, \quad (1)$$

where $\hat{H}_c = \hbar\omega\hat{c}^\dagger\hat{c}$ represents the photonic mode, $\hat{H}_m = \hbar\omega_m\hat{b}^\dagger\hat{b}$ the magnon mode, and $\hat{H}_{\text{int}}$ is the Zeeman interaction [21], which describes the coupling between the two oscillators for this system. $\hbar$ is the reduced Planck constant, $\omega_{c(m)}/2\pi$ is the cavity (magnon) frequency, and $\hat{c}^\dagger$ and $\hat{c}$ ($\hat{b}^\dagger$ and $\hat{b}$) are the creation and annihilation cavity (magnon) operators, respectively.

Following [21], and as demonstrated in Appendix A, the physics system is described by the Dicke model reading as

$$\hat{H}/\hbar = \omega\hat{c}^\dagger\hat{c} + \omega_m\hat{b}^\dagger\hat{b} + g(\hat{c}^\dagger + \hat{c})(\hat{b}^\dagger + \hat{b}). \quad (2)$$

An easy way to solve eigenvalues of the Dicke Hamiltonian is to use the rotating-wave approximation (RWA), where the counter-rotating terms, $\hat{c}^\dagger\hat{b}^\dagger$ and $\hat{c}\hat{b}$, are neglected. In the case of a system being in the USC regime, it is well known [14,15] that this approximation no longer describes this system. Using the Hopfield-Bogoliubov transformation allows one to solve for the system eigenfrequencies while considering corotating, $\hat{c}^\dagger\hat{b}$ and $\hat{c}\hat{b}^\dagger$, and counter-rotating terms:

$$\omega_\pm = \frac{1}{\sqrt{2}}\sqrt{\omega^2 + \omega_m^2 \pm \sqrt{\left(\omega^2 - \omega_m^2\right)^2 + 16g^2\omega\omega_m}}. \quad (3)$$

Moreover, the coupling strength is defined as [29]

$$\frac{g}{2\pi} = \frac{\gamma}{4\pi}\eta\sqrt{\frac{\mu_0 S\hbar\omega}{V_m}} = \eta\sqrt{\omega}\frac{\gamma}{4\pi}\sqrt{\frac{\mu}{g_l\mu_B}\mu_0\hbar n_s}, \quad (4)$$

where $\gamma = 2\pi\,28$ GHz T^{-1} is the gyromagnetic ratio for YIG, $g_l = 2$ is the Landé g factor for an electron spin, μ_0 is the vacuum permeability, μ_B is the Bohr magneton, $\mu = 5\mu_B$ is the magnetic moment of the sample, $n_s = 4.22 \times 10^{27}$ m^{-3} is the spin density for YIG [29], and η is the filling factor, where

$$\eta = \sqrt{\frac{\left(\int_{V_m}\mathbf{h}\cdot\hat{x}dV\right)^2 + \left(\int_{V_m}\mathbf{h}\cdot\hat{y}dV\right)^2}{V_m\int_{V_c}|\mathbf{h}|^2dV}}. \quad (5)$$

The filling factor describes the proportion of the **h** field (x- and y-axis components) perpendicular to the static magnetic field (**H** field), named $\mathbf{H}_0$ in Fig. 1, compared to the **h** field for all directions inside the entire cavity volume V_c.

III. OPTIMIZATION

An appropriate optimization of the cavity allows one to maximize the coupling and to obtain a quasihomogeneous **h** field inside the YIG slab. With the use of finite-element modeling (FEM) and following the procedure described by Bourhill *et al.* [29], we were able to precisely predict, and therefore optimize prior to construction, the cavity frequency, frequency tuning range, and the coupling strength considering Eq. (4).

The optimization of the cavity design was based on the maximization of the filling factor η and the **h**-field homogeneity at the first BM inside the YIG slab. For a correct distribution of the rf field inside the cavity (seen as a perfect electric conductor, PEC), it is necessary to consider the electrical property of the YIG, namely, a relative dielectric permittivity of 15. Dynamic magnetic properties are not useful at this stage, and instead of considering the magnetic permeability with the Polder tensor, we consider it as that of vacuum.

The optimization was carried out for a fixed value of the distance d between the posts and the lid of the cavity ($d = 50$ μm). Then there exist only three free parameters for the optimization of the hybrid system, two for the size of the posts, the width W, and the length L, and one for the cavity, the radius R. The other parameters, such as the height of the cavity and the distance between the posts, were fixed by the constraints imposed by the YIG dimension and the cavity manufacturing accuracy. The optimization step is described in Appendix B, and the optimized values are $W = 0.6$ mm, $L = 6$ mm, and $R = 12$ mm.
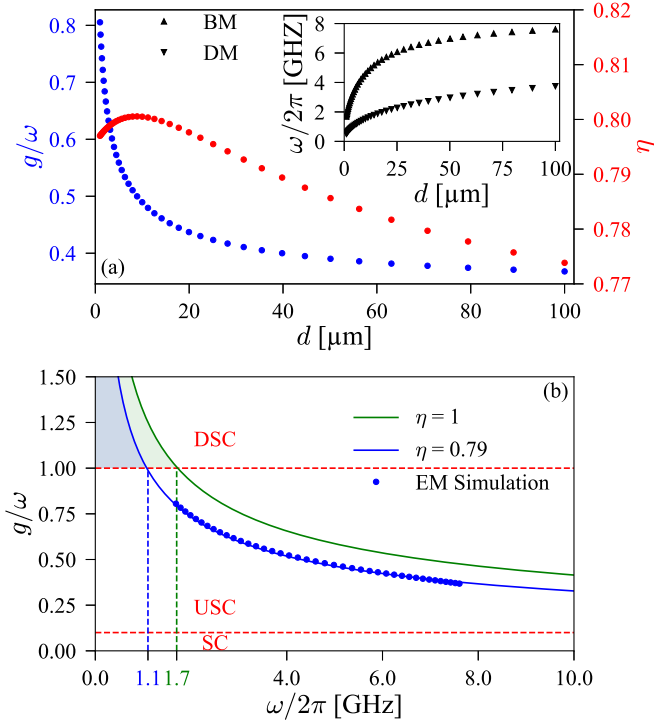
FIG. 2. (a) Evolution of the ratio g/ω (with $\omega = \omega_{BM}$) in blue and η in red vs d for eigenmode simulations (EM). Inset: Evolution of simulated DM and BM frequencies vs d. (b) Evolution of g/ω vs the BM frequency for $\eta = 1$ and $\eta = 0.79$.

The simulated evolution of the two eigenmodes (DM and BM) are shown in the inset of Fig. 2(a) with respect to the distance d, with a range from 1 to 100 μm. Decreasing d will decrease the frequency of the eigenmodes and the frequency difference between the BM and the DM. Figure 2(a) shows electromagnetic simulation results for η (right y axis) and g/ω (left y axis) versus d for a cavity with the optimized dimensions, where $\omega = \omega_{BM}$, the frequency mode of interest in our study. η is maximized for $d = 9$ μm. The variation of η over this range of d values is only is 2.7%, and therefore we may consider it more or less invariant. The tunability of the distance d plays a role on the g/ω ratio, as shown in Fig. 2(a). Indeed, $\omega/2\pi$ is decreasing with d, and η is remaining almost constant. Considering Eq. (4), $g/2\pi$ is a function of η and the square root of ω. Therefore, the ratio g/ω will increase with the inverse of the square root of ω from 36.8% to 80.5% as d decreases from 100 to 1 μm.

Figure 2(b) illustrates the SC to DSC transition for YIG with the frequency dependence of g/ω. The blue dots correspond to the values extracted from EM simulation already discussed in Fig. 2(a), and the solid line dependencies are based on Eq. (4) for two constant values of η, 0.79 (blue) and 1 (green). The magnetic properties of YIG require working in a specific frequency range in order to explore the DSC. For the maximum reachable value of η (green line), which corresponds to the entire **h**-field perpendicular to $\mathbf{H}_0$ and fully confined to $\mathbf{V}_m$, DSC is possible when the magnons are coupled to a microwave mode below 1.72 GHz [29]. In our case (with η close to 0.79), DSC is achievable but at a smaller resonant frequency (1.07 GHz). Note that the optimized cavity

configuration of this work does not allow to reach the DSC due to the presence of the dark mode, which prevents clear identification of the coupling signature in the spectra when the DM and BM are close, and the difficulty to control distance d lower than 3 μm.

IV. RESULTS AND DISCUSSION

A. Simulation details

To compare the experimental results, simulations in the frequency domain (FD), solving for the S_{21} scattering parameter, were conducted for different values of d from 2 to 100 μm. For these simulations we considered the excitation probes and hence the coupling losses. Losses due to finite conductivity of the cavity walls are also taken into consideration.

The static and dynamic magnetic properties of YIG are used to solve the frequency response of the entire system as a function of the applied magnetic field. The spin dynamics of ferrimagnetic systems can be described by the Landau-Lifshitz-Gilbert (LLG) equation, and the frequency dependence of the coupled dynamics can be accurately estimated by using a linear solution of the LLG equation in solving Maxwell's equations. Some consideration regarding the shape of the YIG sample must be taken into account. The FMR dispersion for a relatively thick slab geometry requires careful consideration. Based on the works of Kittel [30], and Joseph and Schlömann [31], the demagnetizing field expression has been adapted to our nonellipsoidal sample of YIG (as described in Appendix B). From these results it is determined that the demagnetizing field is significantly different from the thin-film form, and therefore for accurate simulations proper consideration of this difference must be taken into consideration. Hence, the effective static magnetic field in the YIG is different from the applied one and is read as

$$H_i = H_0 - N_{zz}(x, y, z)M_0, \qquad (6)$$

where H_i is the internal static magnetic field along the z axis, and N_{zz} is the spatially dependent demagnetizing component along the z axis, and is described in Eq. (C3) in Appendix C.

B. Experimental setup

To reach the specifications described above, an aluminum cavity with an accuracy of 20 μm has been machined.

For the applied static magnetic field, we used an electromagnet where the produced field is aligned along the z axis (see Fig. 1) in the direction of the height of the posts. $\mathbf{H}_0$ aligns all the spin moments along the z axis and to saturate the macroscopic YIG magnetization. With the shape of the cavity, the **h** field for the BM, considered as the perturbative field, is only along the x axis inside the YIG slab between the two posts, as shown in Fig. 1(b), due to the constructive interference of the two **h** fields around each post. A gauss meter allows one to measure *in situ* $\mathbf{H}_0$ magnitudes. S parameters are measured with a two-port vector network analyzer (VNA), with the magnitude and phase of the scattering parameters recorded between 0.1 and 15 GHz with an input power of -10 dBm. All measurements were conducted at RT.

The magnitudes of the S_{21} transmission spectra as a function of H_0 are displayed in Fig. 3 for measurement and
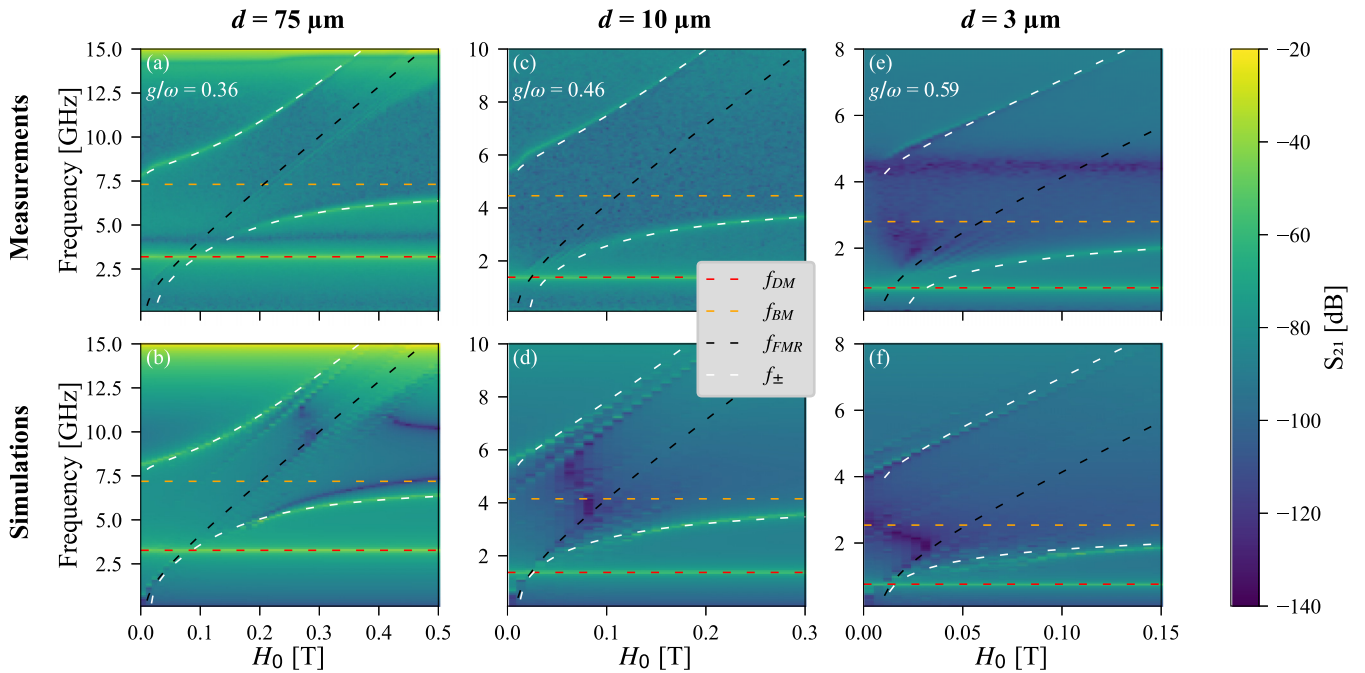
FIG. 3. Transmission spectra vs frequency and H_0 for (a), (c), (e) measurements at RT, and (b), (d), (f) simulations. Comparison spectra between measurement and simulations are shown for different distances d as labeled. A fit with the Dicke model with a shifted magnon frequency is shown superimposed on (c) and (d) where the FMR frequency ($f_{FMR} = \omega_{FMR}/2\pi$) is shown in black, the DM frequency ($f_{DM} = \omega_{DM}/2\pi$) in red, the BM frequency ($f_{BM} = \omega/2\pi$) in orange, and the two polariton frequencies ($f_{\pm} = \omega_{\pm}/2\pi$) in white.

simulation, with differing sized gaps between the top of the posts and the roof of the cavity. Experimentally, this is varied by using different cavity lids which had recesses of differing heights machined into them.

C. Results

Measurement and simulation results of magnetic spectroscopy of the cavity-magnon system are shown in Fig. 3 as the first and second row, respectively, for different values of d. Each column represents a comparison between a measurement and a simulation with a distance close to the measured value. The latter can be determined by the unperturbed value of f_{DM}, which acts as a calibration for d.

The external magnetic field was always applied symmetrically for negative and positive values. This allows us to improve the fit accuracy on measurements, because we have twice as many data points. All measurements with complete frame are shown in Appendix F.

We can easily distinguish the two hybrid eigenfrequencies $f_+ = \omega_+/2\pi$ (for the higher branch) and $f_- = \omega_-/2\pi$ (for the lower branch) from either side of the BM frequency. It should be noted that at low H_0 values the BM is not visible, while we can clearly see the DM which is the lowest frequency mode and has a negligible coupling with the magnon mode and hence is constant versus H_0.

Some minor discrepancies between simulation and experiment should be pointed out: (i) an inflection point on the curvature of the upper CMP in frequency at low H_0 (observed only in the USC regime) for measurements, appearing neither in simulation nor analytic fits; (ii) antiresonances only appearing either in measurement, the horizontal one around

4.3 GHz in Figs. 3(a) and 3(e), or in simulation with a S-like shape, around 10, 4, and 2 GHz in Figs. 3(b), 3(d), and 3(f), respectively. Let us notice that this antiresonance does not appear in measurements when a cavity mode is overlapping with this transmission dip, as shown for $d = 10$ μm in Fig. 3(c) and Fig. 9(e), and for $d = 116$ μm in Fig. 9(a); (iii) another magnon mode exists near the upper CMP in simulations. It is clear that it is another magnon mode because its **H** field's frequency dependence does not change as d is varied.

Differences given in the two last points could be explained by the fact that the YIG sample is a perfect rectangular prism in simulation whereas the real sample is not. The imperfections of the YIG geometry could result in a weak transmission, which could be not detected in measurement.

Despite these minor deviations, the agreement between simulations and measurements on the magnon-photon coupling and the resulting CMPs is excellent. In particular, we validated the spatial distribution of the demagnetizing field, hence the expression of the FMR for a slab and the ability of the Maxwell's equations to describe the system. This permits one to conduct a simulation with a magnetic field larger than experimentally possible in order to extract the BM frequency. Indeed, it is impossible to measure the unperturbed BM frequency f_{BM} in the USC regime even when applying a high magnetic field near 2 T.

D. Model description

In the USC regime, the Tavis-Cummings model becomes no longer applicable [13,32], as $g/\omega > 0.1$ leads to a failure of the rotating-wave approximation as the interaction term of the Hamiltonian can no longer be assumed to be "slowly rotating"
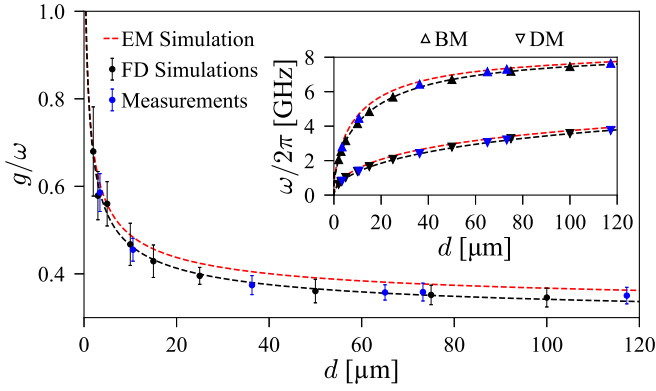
FIG. 4. g/ω vs d for fitted FD simulations (in black) and for fitted measurements (in blue). The simulation trend is plotted in the black, dashed line. Inset: DM and BM frequencies vs the distance d in the black dashed line are shown DM and BM reading values from simulations at extremely high applied **H** field. Eigenmode (EM) simulations are shown as the red dashed line.

compared to the system terms. The standard model for cavity magnonics is the Dicke model [see Eq. (2)]. However, we have noticed that in the coupling regime of our system, even the Dicke model cannot describe observed polariton frequency dispersion for measurements and simulations, as shown in Fig. 7 in Appendix D. Another standard model describing light-matter interactions is the Hopfield model [33], similar to the Dicke model with an additional diamagnetic term. This well-known model also did not fit the measured data, as shown in Appendix E.

To remedy these issues, it has been proposed to modify the Dicke model with the addition of an **H** field in the FMR dispersion equation [22]. We also modified the term of the FMR frequency dependence in Eq. (3) to

$$\omega_m \to \omega_m + \Delta_m, \tag{7}$$

where $\Delta_m = 2\pi f_\Delta$ is a frequency shift, which is further discussed in Sec. IV E. This modified Dicke model was found to fit best the experimental and simulation spectra, as seen in the white dashed lines of Fig. 3 for $d = 75$ μm in (a) and (b), $d = 10$ μm in (c) and (d), and $d = 3$ μm in (e) and (f). Measurement fit, shown in Figs. 3(a), 3(c), and 3(e), is achieved with the BM frequency f_{BM} (in orange), the coupling strength $g/2\pi$, and the added frequency f_Δ as fitting parameters. For simulation fit, shown in Figs. 3(b), 3(d), and 3(f), the BM frequency is considered as a fixed parameter. Indeed, simulations were performed at an artificially high **H** field ($H_0 = 10$ T) in order to tune the magnon mode many orders of coupling strength away and clearly distinguish the two photonic modes.

An offset far detuned from the BM frequency at a zero **H** field arises for high g/ω when the FMR is shifted. When the FMR is not shifted, in the standard Dicke model, no BM frequency detuning at zero **H** field exists for any g/ω value. See Appendix G for more details about the frequency detuning at zero **H** field.

All values of fit parameters, for measurements and simulations, are available in Appendix F and are pooled in Fig. 4. For the measurements (shown in blue), the distance d has

TABLE I. Operating range of the cavities.

Cavity	f_{BM} [GHz]	$g/2\pi$ [GHz]	$\Delta_m/2\pi$ [GHz]
CAV_{01}	2.80–7.65	1.64–2.68	2.27–2.59
CAV_{02}	7.63–9.79	2.42–2.72	1.63–1.74
CAV_{03}	2.35–5.53	0.58–0.69	0.29–0.50

been estimated from the measured DM frequency. The fitted BM frequencies of the measurements are in good agreement with simulations (shown in black in the inset of Fig. 4). Regarding the coupling strength g/ω, we achieve a ratio g/ω ranging from 0.35 to 0.59, corresponding to $d = 116$ μm to $d = 4$ μm, respectively. As mentioned in Sec. III, the values of g/ω are different from the optimization step values (dotted red curve), mainly due to the different estimated frequencies, shown in the inset. Once again, the correlations between fitted simulations and measurements for the ratio g/ω are also good. This clearly demonstrates the validity of the simulations.

E. Discussion

We discuss here the physical meaning of the frequency shift in the modified Dicke model. For a deeper understanding of the behavior of this added term, we investigated the transition between the SC and the USC regimes. In order to study a wide range of g/ω values, we have used two other cavities with the same YIG sample. The first described machined cavity will be named "CAV_{01}" in the following. This cavity operates in a g/ω range from 0.35 to 0.59, as mentioned in Table II in Appendix F.

The second cavity, "CAV_{02}," has been 3D printed and has the same shape as CAV_{01} but with smaller height posts. This cavity is performing in a certain range of g/ω, from 0.28 to 0.32 (see Table III in Appendix F).

The third cavity, "CAV_{03}," is also a double reentrant 3D-printed cavity with cylinder posts, adjustable in height. This cavity was used in a previous work [29] to experimentally verify a reworked theory that predicts coupling values from simulations alone. The cavity has radius $R_{cav} = 20$ mm and height $H_{cav} = 4.6$ mm, while the posts have radius $R_{post} = 2.05$ mm and are spaced to 2.7 mm. The operating ratio g/ω is lower than the two other cavities and enables us to have experimental results at the SC/USC threshold, with g/ω comprised between 0.12 and 0.25 (see Table IV in Appendix F).

The operating range in BM frequencies, coupling strengths, and added frequencies for the three cavities are summarized in Table I.

Thanks to the validation of the FD simulations, we were able to simulate the CAV_{01} design for different dimensions of the YIG slab while keeping the aspect ratio of the slab constant. Since the demagnetizing components described in Eq. (C3) are only dependent on this aspect ratio, the FMR remains unchanged. However, still decreasing the YIG slab dimensions decreases the filling factor η, and therefore the coupling strength and g/ω from 63% to 5% with $d = 50$ μm.

We plotted Δ_m/ω vs g/ω in Fig. 5(a), which clearly display a quadratic dependence. For $g/\omega \leqslant 0.1$, Δ_m/ω is more or less negligible. This description agrees with the commonly situated transition point (shown as the red dotted line)

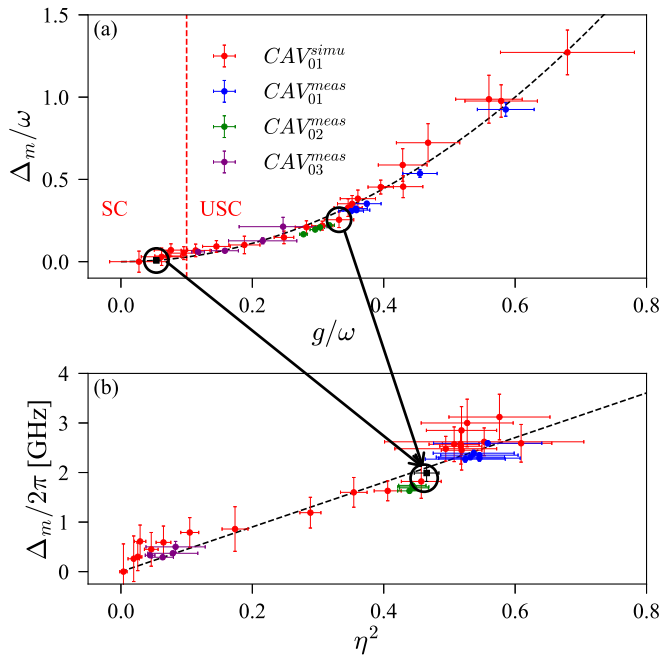FIG. 5. (a) Δ_m/ω vs g/ω and (b) $\Delta_m/2\pi$ vs η^2. Shown are the FD simulations on CAV_{01} in red and measurements in blue, in green for CAV_{02}, and in purple for CAV_{03}. In (a) and (b), fitted values for a reduced CAV_{01} with an aspect ratio equal to 0.025 as the black square. The two data points circled in (a) correspond to the same value of $\Delta_m/2\pi$ in (b).

between the SC and USC regimes where all models converge. Our simulations show the need for the $\Delta_m/2\pi$ parameter to properly fit the data. Figure 5(b) shows that $\Delta_m/2\pi$ is linearly proportional to η^2. According to this observation and the definition of η, we noticed that the more this energy is confined in the YIG, the larger the shift in the magnon frequency will be. In the literature, the parameter η is not so often considered or estimated. In Ref. [29] we had the opportunity to test the model of Eqs. (4) and (5) on multiple published experimental results, and η rarely exceeds 0.05 in any of them. As a reminder, and in view of the description in Fig. 2, our system (CAV_{01}) proposes an η of about 0.79.

In Fig. 5 is represented by square marker a simulation where dimensions of the cavity and the YIG are reduced by a ratio equal to 0.025 for $d = 50$ μm. By decreasing the dimensions of the entire cavity CAV_{01} by this ratio, the BM frequency is increased to 275 GHz. Then this cavity operates in the SC regime. However, the proportion of the **h** field in the YIG remains the same, hence also η.

In Fig. 5(a) are circled the reduced system performing in the SC regimes and the unmodified cavity in the USC regime presenting the same η value. In Fig. 5(b) it is shown that the frequency shift $\Delta_m/2\pi$ is the same for both cavities, and for the same value of η^2. It is then important to note that this effect is not bounded to the coupling strength and hence to the coupling regime but instead to the filling factor, something that has never been discussed so far.

Considering Eq. (4), $\Delta_m/2\pi$ is also linearly proportional to g^2/ω, which is a dependent function of the magnetic properties of the YIG and η^2. As a physical mechanism we have

identified two nonlinear processes that could be involved in the appearance of $\Delta_m/2\pi$ in this study due to their similar behavior: the multiphoton Rabi oscillations [14,34,35] for its effective coupling being proportional to g^2/ω. When the coupling between an artificial single atom and a cavity is in the USC regime, the system can exchange several photons (and undergo multiphoton Rabi oscillations) instead to a single one (commonly known as Rabi oscillation); and the self-Kerr, and the cross-Kerr effects [36–40] presenting a frequency shift of the magnon, due to magnetocrystalline anisotropy and magnon-magnon interactions, respectively.

V. CONCLUSION

In conclusion, we proposed a double reentrant cavity design to achieve USC magnon/photon coupling at microwave frequencies, which was supported by both experimental data and electromagnetic simulations. This is a demonstration of USC magnon/photon coupling at room temperature. Achieving the USC without cryogenic temperature is promising for the development of rf applications based on cavity spintronics.

We explained the importance of optimizing the filling factor η for reaching the USC, aside from just the frequency of the resonator and the spin density. Importantly, the cavity we proposed is parametrized by the distance d between the posts and the lid. We showed that tuning this parameter allowed us to continuously go from the regular SC to the USC regime. The ability to study the transition from the SC to USC regime is a significant step towards understanding the physics of USC magnon/photon coupling.

Indeed, we showed that the standard models describing the coupling of a single resonator mode to many dipoles (e.g., the Dicke and Hopfield models) failed to properly describe our experimental data. Nevertheless, thanks to the validation of our electromagnetic simulations, we showed that a frequency shift in the magnon frequency adequately modelled our data, which we note is fully captured by the classical Maxwell equations. Furthermore, we showed that this frequency shift only depended on the filling factor η, highlighting its importance for hybrid magnon/photon systems. While the physical origin of the magnon's frequency shift is still unknown, we hope that its relation with η will motivate further research into deriving a proper theoretical model for USC magnon/photon coupling.

APPENDIX A: PHYSICS DESCRIPTION

The system under consideration is best described by the Hamiltonian of two coupled harmonic oscillators. The oscillators represent the cavity photonic mode $\hat{H}_c = \hbar\omega\hat{c}^\dagger\hat{c}$ and the uniformly precessing Kittel magnon mode $\hat{H}_m = \hbar\omega_m\hat{b}^\dagger\hat{b}$, where $\hbar$ is the reduced Planck constant, $\omega/2\pi$ and $\omega_m/2\pi$ are respectively the cavity and magnon frequencies, and $\hat{c}^\dagger$ ($\hat{b}^\dagger$) and $\hat{c}$ ($\hat{b}$) are the creation and annihilation cavity (magnon) operators. The coupling is then read as a an interaction $\hat{H}_{int}$, and the entire system Hamiltonian can then be written as

$$\hat{H} = \hat{H}_c + \hat{H}_m + \hat{H}_{int}. \tag{A1}$$

The quantization of Maxwell's equation leads to the expression of the vector potential,

$$\hat{\mathbf{A}}(\mathbf{r}, t) = \sum_n \frac{\hat{q}_n(t)}{\sqrt{\epsilon_0\epsilon_{r,n}}}\mathbf{U}_n(\mathbf{r}), \tag{A2}$$

where ϵ_0 is the vacuum permittivity, $\epsilon_{r,n}$ the relative permittivity experienced by the cavity mode n, $\hat{q}_n(t)$ is the temporal term, and $\mathbf{U}_n(\mathbf{r})$ is the space-dependent operator. This expression is generalized for all modes in a cavity. In the following we will concern ourselves with only a single mode.

This potential vector in a cavity is comparable to a simple harmonic oscillator, where radiation modes are defined according to annihilation and creation operators:

$$\hat{c} = \frac{1}{\sqrt{2\hbar\omega}}(\omega\hat{q} - i\hat{q})$$

$$\hat{c}^\dagger = \frac{1}{\sqrt{2\hbar\omega}}(\omega\hat{q} + i\hat{q}). \tag{A3}$$

Then the rf magnetic field (**h** field) bounded to the cavity mode is [41]

$$\hat{\mathbf{h}} = \frac{1}{\mu_0}\nabla \times \hat{\mathbf{A}} = \frac{1}{\mu_0}\sqrt{\frac{\hbar}{2\omega\epsilon_0\epsilon_{r,c}}}(\hat{c}^\dagger + \hat{c})\nabla\times\mathbf{U}, \tag{A4}$$

where μ_0 is the vacuum permeability, ϵ_0 the vacuum permittivity, $\epsilon_{r,c}$ the relative permittivity experienced by the cavity mode, and $\mathbf{U}$ is the space-dependent operator of the potential vector. The component of this field perpendicular to the sample's magnetization direction will couple to the Kittel magnon mode.

For such a uniform precession of the magnetic sample, we introduce the macrospin operator considering the entire sample as

$$\hat{\mathbf{S}} = \frac{V_m}{\gamma}\hat{\mathbf{M}}, \tag{A5}$$

where $\hat{\mathbf{M}}$ is the magnetization operator, V_m the volume of the magnetic sample, and γ the gyromagnetic ratio.

We consider a saturated magnetization by the use of an applied static magnetic field (**H**-field) in the z-axis direction. It is then useful to introduce spin raising $\hat{S}^+$ and lowering $\hat{S}^-$ operators. Following the Holstein-Primakoff transformation [42] and considering low excitation numbers vs the total spin

number of the macrospin operator, we obtain

$$\hat{S}^+ = \hat{S}_x + i\hat{S}_y = \sqrt{2S - \hat{b}^\dagger\hat{b}\hat{b}} \approx \sqrt{2S}\hat{b}$$

$$\hat{S}^- = \hat{S}_x - i\hat{S}_y = \hat{b}^\dagger\sqrt{2S - \hat{b}^\dagger\hat{b}} \approx \sqrt{2S}\hat{b}^\dagger \tag{A6}$$

$$S_z = S - \hat{b}^\dagger\hat{b},$$

where $S = \frac{\mu}{g_l\mu_B}N_s$ is the total spin number of the macrospin, μ_B is the Bohr magneton, μ is the magnetic moment of the sample, g_l is the Landé g factor, and $N_s = n_sV_m$ is the number of spins in the sample, with n_s the spin density.

The interaction term corresponds in this case to the Zeeman energy:

$$\hat{H}_{int} = -\mu_0 \int_{V_m} \hat{\mathbf{M}} \cdot \hat{\mathbf{h}}dV. \tag{A7}$$

Substituting $\hat{\mathbf{h}}$ and $\hat{\mathbf{M}}$ in Eq. (A7) by their expressions in Eqs. (A4) and (A5), and replacing Cartesian macrospin values by raising and lowering ones, with neglecting z-axis terms, we arrive at

$$\hat{H}_{int}/\hbar = g_x(\hat{c} + \hat{c}^\dagger)(\hat{b} + \hat{b}^\dagger) + ig_y(\hat{c} + \hat{c}^\dagger)(\hat{b} - \hat{b}^\dagger), \tag{A8}$$

where the coupling strengths are defined as

$$g_x = -\frac{\gamma}{2V_m}\sqrt{\frac{\hbar S}{\omega\epsilon_{r,c}\epsilon_0}} \int_{V_m} (\nabla \times \mathbf{U}) \cdot \hat{x}dV$$

$$g_y = \frac{\gamma}{2V_m}\sqrt{\frac{\hbar S}{\omega\epsilon_{r,c}\epsilon_0}} \int_{V_m} (\nabla \times \mathbf{U}) \cdot \hat{y}dV. \tag{A9}$$

In order to consider the integration of the $\nabla \times \mathbf{U}$ term in the magnetic sample volume in x and y axis, it is necessary to rewrite it considering the entire **h** field "seen" by the sample. Therefore it is convenient to normalize the **h** field against that of the entire cavity. The classical expression for the **h**-field energy for a single cavity mode is

$$\mathcal{E} = \frac{\mu_0}{2}\int \mathbf{h} \cdot \mathbf{h}dV$$

$$= \frac{\mu_0}{2\epsilon_0\epsilon_{r,c}}q \cdot q \int (\nabla \times \mathbf{U}) \cdot (\nabla \times \mathbf{U})dV, \tag{A10}$$

where $\int_{V_c}(\nabla \times \mathbf{U}) \cdot (\nabla \times \mathbf{U}) = \frac{\epsilon_{r,c}\omega^2}{c^2}$ [41].

Regarding the ratio of the **h**-field energy in the magnetic sample versus the one in the whole cavity, we get

$$\frac{\mathcal{E}_{V_m}}{\mathcal{E}_{V_c}} = \frac{\int_{V_m} \mathbf{h} \cdot \mathbf{h}dV}{\int_{V_c} |\mathbf{h}|^2dV} = \frac{\int_{V_m} (\nabla \times \mathbf{U}) \cdot (\nabla \times \mathbf{U})dV}{\epsilon_{r,c}\omega^2/c^2}. \tag{A11}$$

Using the center and right terms of the above equation, deriving numerators and applying the square root, we finally read the infinitesimal normalized energy amplitude of the **h** field:

$$\nabla \times \mathbf{U} = \frac{\sqrt{\epsilon_{r,c}}\omega}{c}\frac{\mathbf{h}}{\sqrt{\int_{V_c} |\mathbf{h}|^2dV}}. \tag{A12}$$

Equation (A1), with the use of Eq. (A8), can be rewritten over a matrix form as

$$\hat{H} = \frac{1}{2} [\hat{c}^\dagger \quad \hat{b}^\dagger \quad \hat{c} \quad \hat{b}] H [\hat{c}^\dagger \quad \hat{b}^\dagger \quad \hat{c} \quad \hat{b}]^\dagger + const$$

$$H = \begin{bmatrix} \omega & g_x + ig_y & 0 & g_x - ig_y \\ g_x - ig_y & \omega_m & g_x - ig_y & 0 \\ 0 & g_x + ig_y & \omega & g_x - ig_y \\ g_x + ig_y & 0 & g_x + ig_y & \omega_m \end{bmatrix}.$$

$$(A13)$$

Using Hopfield-Bogoliubov transformation [22], the solution of the problem is to find polariton operators $\hat{p}_\pm$, expressed as a linear combination of $\hat{c}$, $\hat{c}^\dagger$, $\hat{b}$, and $\hat{b}^\dagger$. Being bosonic operators, they should obey the Hopfield formulation [33]:

$$[\hat{p}_\pm, \hat{H}] = \omega_\pm \hat{p}_\pm, \quad (A14)$$

where $\omega_\pm/2\pi$ are frequency eigenvalues associated with the eigenoperators $\hat{p}_\pm$.

As previously, the Hamiltonian in the polaritonic basis can be rewritten as

$$\hat{H} = \frac{1}{2} [\hat{p}_-^\dagger \quad \hat{p}_+^\dagger \quad \hat{p}_- \quad \hat{p}_+] M [\hat{p}_-^\dagger \quad \hat{p}_+^\dagger \quad \hat{p}_- \quad \hat{p}_+]^\dagger.$$

$$(A15)$$

In order to respect Eq. (A14), the Hopfield matrix M has to be read as

$$M = H \text{diag}(1, 1, -1, -1). \quad (A16)$$

Solving eigenvalues of the matrix M leads to

$$\omega_\pm = \frac{1}{\sqrt{2}} \sqrt{\omega^2 + \omega_m^2 \pm \sqrt{(\omega^2 - \omega_m^2)^2 + 16g^2 \omega \omega_m}}, \quad (A17)$$

where the coupling strength $g = \sqrt{g_x^2 + g_y^2}$ is defined as

$$\frac{g}{2\pi} = \frac{\gamma}{4\pi} \eta \sqrt{\frac{\mu_0 S \hbar \omega}{V_m}} = \eta \sqrt{\omega} \frac{\gamma}{4\pi} \sqrt{\frac{\mu}{g_l \mu_B} \mu_0 \hbar n_s} \quad (A18)$$

with the filling factor

$$\eta = \sqrt{\frac{\left(\int_{V_m} \mathbf{h} \cdot \hat{x} dV\right)^2 + \left(\int_{V_m} \mathbf{h} \cdot \hat{y} dV\right)^2}{V_m \int_{V_c} |\mathbf{h}|^2 dV}}. \quad (A19)$$

It is important to note that eigenfrequencies are a solution of the Dicke model [14,15]. Finally the Hamiltonian can be rewritten over the easier form

$$\hat{H}/\hbar = \omega \hat{c}^\dagger \hat{c} + \omega_m \hat{b}^\dagger \hat{b} + g(\hat{c}^\dagger + \hat{c})(\hat{b}^\dagger + \hat{b}). \quad (A20)$$

APPENDIX B: CAVITY OPTIMIZATION

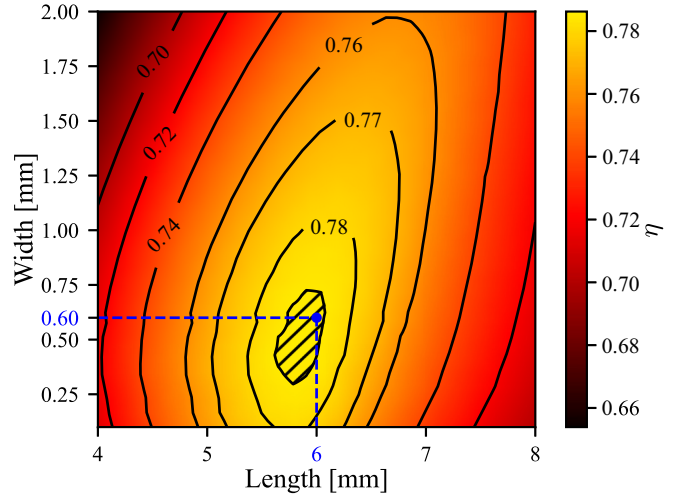Figure 6 is a representation of the optimization of the filling factor η for two of the variable parameters; the width (W) and

FIG. 6. Filling factor η function of the width (W) and the length (L) of the two posts.

the length (L) of the posts, with d chosen equal to 50 μm. The cavity radius (R) has been chosen at its optimized value. The containment of the **h** field inside the YIG is at its maximum when the post dimensions are of the slab dimensions. Hence the width of the posts has been optimized over a range from 0.1 to 2 mm and their lengths from 4 to 8 mm. The radius of the cavity does not have a big impact on η. The cavity radius has been optimize over a range from 10 to 14 mm.

Each contour represents the value of η with respect to W and L. The hashed contour delimits the surface where $\eta \geqslant 78.5\%$. For better feasibility, we choose the largest values of W and L. This leads to an optimal value of η for $W = 0.6$ mm, $L = 6$ mm, and $R = 12$ mm.

APPENDIX C: FMR MODEL

Using the Landau-Lifshitz equation of the magnetization with the proper approximations leads us to the FMR pulsation for all types of ferromagnet shapes [30]:

$$\omega_0 = \gamma \sqrt{\left(\frac{\omega_e}{\gamma}\right)^2 - [(N_{xy} + N_{yx})M_s]^2}, \quad (C1)$$

where M_s is the saturation magnetization, $N_{i,j}$ is a component of the demagnetizing tensor at the ith column and the jth row, and ω_e is the FMR pulsation for an ellipsoidal body read as

$$\omega_e = \gamma \sqrt{[|H_z| + (N_{xx} - N_{zz})M_s][|H_z| + (N_{yy} - N_{zz})M_s]}. \quad (C2)$$

Using the perturbation theory with a small perturbation on the **H** field $\epsilon = \frac{M_z}{H_z}$ at the first order, it is shown that the demagnetizing components for a rectangular prism are for the diagonal components [31]:

$$N_{kk}^{(1)} = \frac{1}{4\pi} \left\{ \begin{array}{l} \cot^{-1}[f(x_i, x_j, x_k)] + \cot^{-1}[f(-x_i, x_j, x_k)] \\ + \cot^{-1}[f(x_i, -x_j, x_k)] + \cot^{-1}[f(x_i, x_j, -x_k)] \\ + \cot^{-1}[f(-x_i, -x_j, x_k)] + \cot^{-1}[f(-x_i, x_j, -x_k)] \\ + \cot^{-1}[f(x_i, -x_j, -x_k)] + \cot^{-1}[f(-x_i, -x_j, -x_k)] \end{array} \right\}, \quad (C3)$$
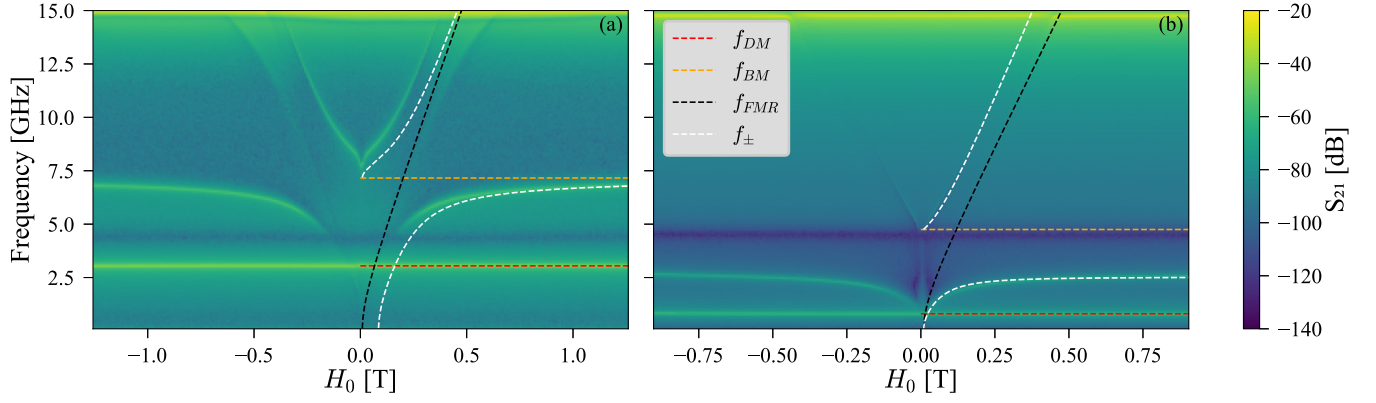
FIG. 7. Transmission spectra vs the rf frequency and the **H** field. Fitted polariton branches are shown in white. The BM frequency (in orange) and the coupling strength are variables. The FMR is shown in black and the DM in red. Fits were be done with the normal phase of the Dicke model. In (a) the measurement for $d = 50$ μm and a fit with the Dicke model. In (b) the measurement for $d = 4$ μm and a fit with the Dicke superradiant phase model.

with

$$f(x_i, x_j, x_k) = \frac{\sqrt{(a_i - x_i)^2 + (a_j - x_j)^2 + (a_k - x_k)^2}(a_k - x_k)}{(a_i - x_i)(a_j - x_j)}, \tag{C4}$$

and for the off-diagonal terms,

$$N_{ik}^{(1)} = -\frac{1}{4\pi} \log \left[\frac{G(\boldsymbol{r}|a_i, a_j, a_k)G(\boldsymbol{r}|-a_i, -a_j, a_k)G(\boldsymbol{r}|-a_i, a_j, -a_k)G(\boldsymbol{r}|a_i, -a_j, -a_k)}{G(\boldsymbol{r}|-a_i, a_j, a_k)G(\boldsymbol{r}|a_i, -a_j, a_k)G(\boldsymbol{r}|a_i, a_j, -a_k)G(\boldsymbol{r}|-a_i, -a_j, -a_k)} \right], \tag{C5}$$

with

$G(\boldsymbol{r}|a_i, a_j, a_k)$

$= (a_j - x_j) + \sqrt{(a_i - x_i)^2 + (a_j - x_j)^2 + (a_k - x_k)^2}.$

$$\tag{C6}$$

Let us notice that the demagnetizing components are spatially dependent and were averaged to x, y, and z equal to zero for analytical equations. For the YIG dimensions mentioned in the manuscript, the off-diagonal components of the demagnetizing tensor are equal to zero and then the slab was the same FMR frequency as read in Eq. (C2).

APPENDIX D: DICKE MODEL

1. Normal phase

The Dicke model is the simplest model to describe the magnon-photon interaction. We consider each Hamiltonian of the cavity photonic mode and magnon as well as the interaction Hamiltonian [22]:

$$\hat{H} = \omega \hat{c}^\dagger \hat{c} + \omega_m \hat{b}^\dagger \hat{b} + g(\hat{c}^\dagger + \hat{c})(\hat{b}^\dagger + \hat{b}). \tag{D1}$$

From this equation we can easily solve for the eigenmodes, that is to say, the polaritronic modes described in Eq. (A17). This equation is only valid when the ratio g/ω is less than 0.5. For a description of a system with a ratio higher than 0.5, it is necessary to use the Dicke superradiant phase [43].

2. Superradiant phase

The superradiant phase is a quantum transition in the Dicke model and represents the displacement of bosonic modes [22]: $\hat{c}^\dagger \to \hat{a}^\dagger + \sqrt{\alpha}$ and $\hat{b}^\dagger \to \hat{d}^\dagger - \sqrt{\beta}$, where α and β represent averaged values of the displaced ground states for the photon and the magnon, respectively. Using Holstein-Primakoff transformation in the Dicke Hamiltonian, the eigenfrequencies become

$$\omega_\pm = \frac{1}{\sqrt{2}}\sqrt{\omega^2 + \tilde{g}^4\omega_m^2 \pm \sqrt{(\omega^2 - \tilde{g}^4\omega_m^2)^2 + 4\omega^2\omega_m^2}}, \tag{D2}$$

where $\tilde{g} = 2\frac{g}{\omega}$.

In this case Fig. 7(b) shows fitted measurement with the superradiant Dicke model. For this fit we do not need to add a frequency term on the FMR, and we found that $\omega = 4.75$ GHz and $g = 2.58$ GHz.

With comparing BM frequencies, DM frequencies, and g as done in Sec. IV C, the BM frequency and g should be higher than those obtained from simulation. Because of this mismatch, it seems that the superradiant phase is not reached. Figure 7 shows transmission spectra with respect to the frequency and the H field. A fit has be done with the standard Dicke model. The two eigenmodes of the fit shown in the dotted white line which are not consistent with the measurement prove the inability to fit with the standard Dicke model.
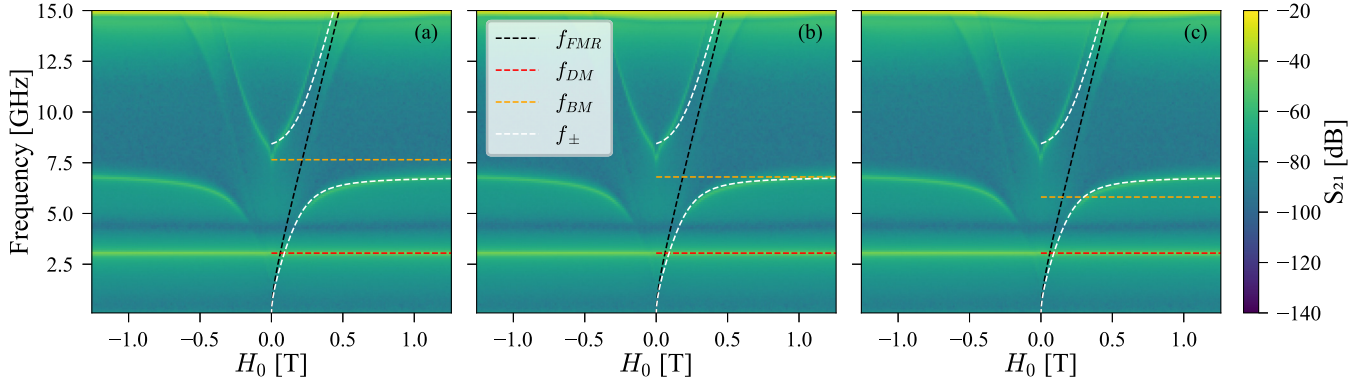
FIG. 8. Transmission spectra vs the rf frequency and the **H** field. Fitted polariton branches are shown in white. The BM frequency (in orange) and the coupling strength are variables. The FMR is shown in black and the DM in red. Fits were be done with the modified Hopfield model where the prefactor is (a) $d < 1$, (b) $d = 1$, and (c) $d > 1$.

APPENDIX E: HOPFIELD MODEL

1. Standard

The Hopfield model is equivalent to the Dicke one with a supplementary term: the diamagnetic one. Considering a carried particle in a magnetic field, we redefine the impulse of the system [22],

$$\hat{p} \rightarrow \hat{p} - q\hat{A}, \tag{E1}$$

with $\hat{A}$ the vector potential and associated to the photonic mode: $\hat{A} \propto (\hat{c}^{\dagger} + \hat{c})$.

We finally have the Hopfield Hamiltonian of the system:

$$\hat{H} = \omega \hat{c}^{\dagger}\hat{c} + \omega_m \hat{b}^{\dagger}\hat{b} + g(\hat{c}^{\dagger} + \hat{c})(\hat{b}^{\dagger} + \hat{b}) + D(\hat{c}^{\dagger} + \hat{c})^2, \tag{E2}$$

where D is the diamagnetic term where the Thomas-Reiche-Kuhn sum rules gives $D = \frac{g^2}{\omega}$.

With using Hopfield-Bogoliubov transformation and redefining g as $g\sqrt{\frac{\omega_m}{\omega}}$ we have

$$\omega_{\pm} = \frac{1}{\sqrt{2}}\sqrt{\omega^2 + \omega_m^2 + 4g^2 \pm \sqrt{\left(\omega^2 + \omega_m^2 + 4g^2\right)^2 - 4\omega^2\omega_m^2}}. \tag{E3}$$

2. Modified

Following Ref. [17], where a prefactor d is added before the diamagnetic term in Eq. (E4), we tried to fit with the modified Hopfield model by varying this prefactor,

$$\omega_{\pm} = \frac{1}{\sqrt{2}}\sqrt{\omega_c^2 + 4dD\omega_c + \omega_c^2 \pm \sqrt{\left(\omega_c^2 + 4dD\omega_c - \omega_m^2\right)^2 + 16g^2\omega_c\omega_m}}, \tag{E4}$$

where $D = g^2/\omega_m$.

Figure 8 shows the fit with the modified Hopfield model when the prefactor is less, equal, or more than 1 in respectively (a), (b), and (c). Let us notice that the standard Hopfield model is for $d = 1$. Finally, the only effect of this prefactor is equivalent to increase (for $d < 1$) or decrease (for $d > 1$) the BM frequency, whereas it is needed to have a model which affects the FMR.
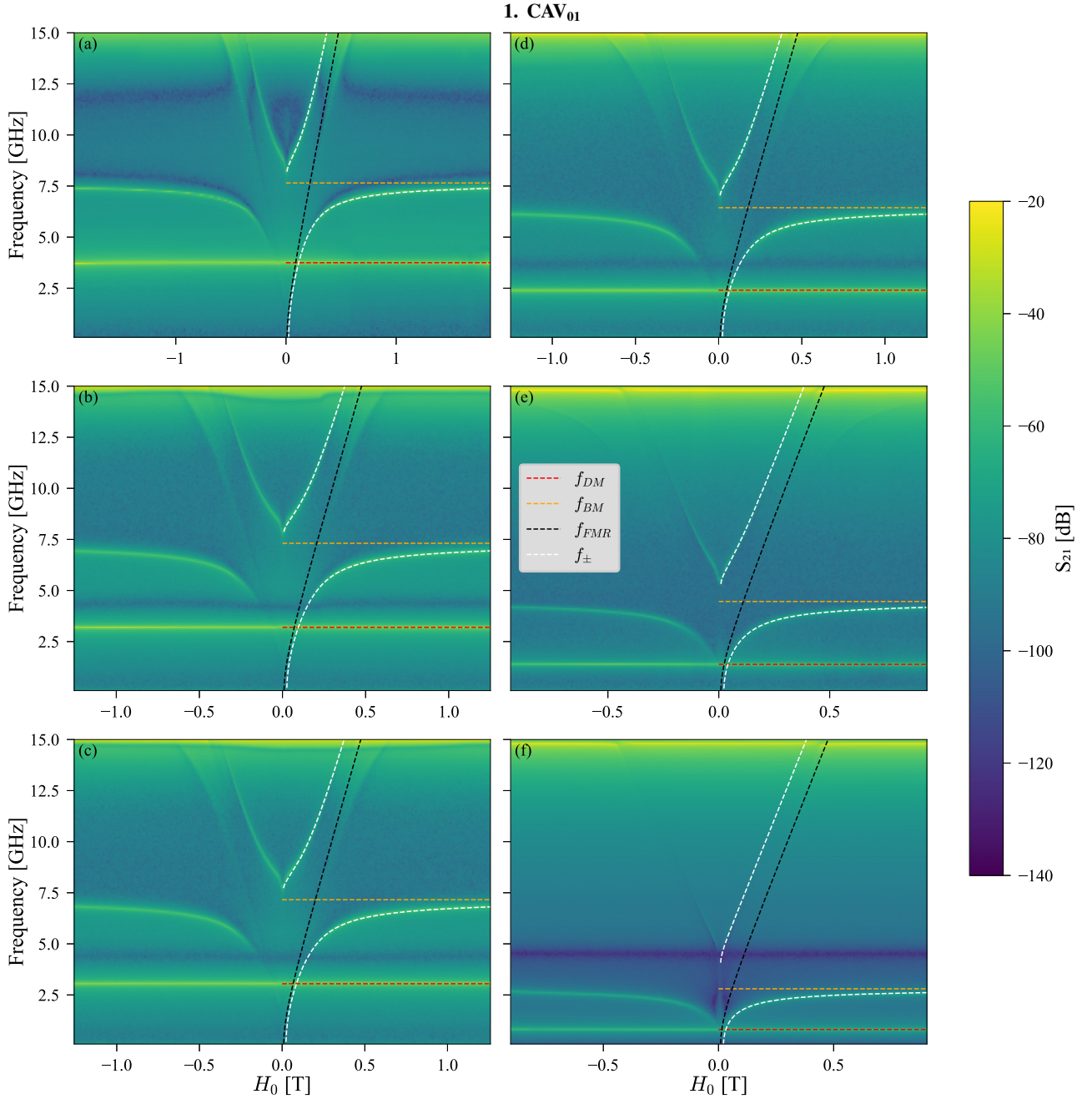
APPENDIX F: MEASUREMENTS

1. CAV$_{01}$

FIG. 9. Transmission spectra vs the rf frequency and the **H** field. Fitted polariton branches are shown in white. The BM frequency (in orange) and the coupling strength are variables. The FMR is shown in black and the DM in red. Fitted parameters are shown in Table II.

TABLE II. The parameters associated with measurements at different values of distance d between the post and the lid of the machined cavity. The numbering refers to the spectra shown in Fig. 9.

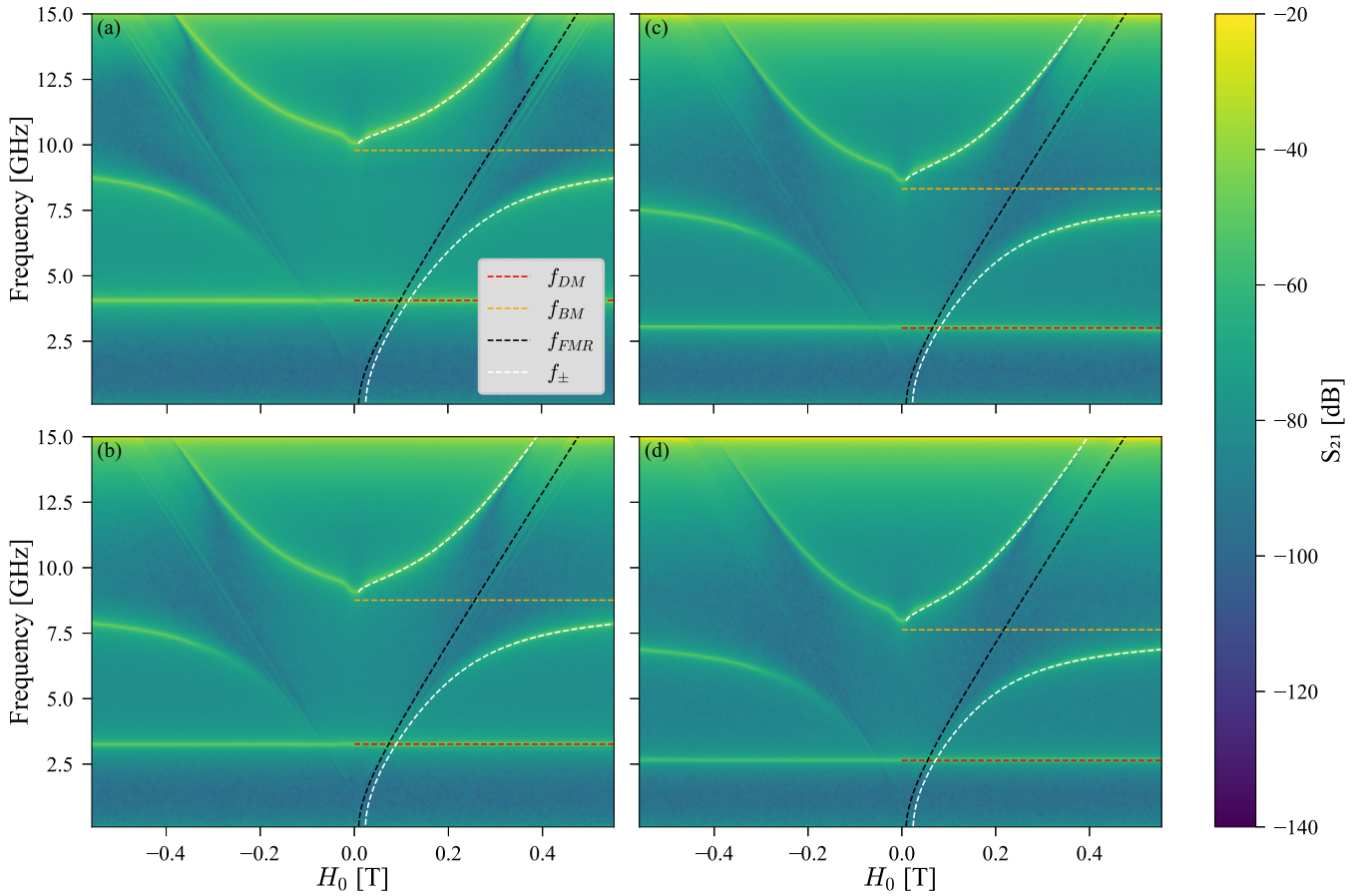| Numbering	d [μm]	f_{DM} [GHz]	f_{BM} [GHz]	$g/2\pi$ [GHz]	g/ω	$g^2/2\pi\omega$ [GHz]	$\Delta_m/2\pi$ [GHz]	f_{gap} [GHz]
(a)	116	3.75	7.65	2.68	0.35	0.94	2.35	0.58
(b)	75	3.19	7.31	2.62	0.36	0.94	2.29	0.54
(c)	65	3.05	7.16	2.56	0.36	0.92	2.31	0.54
(d)	36	2.40	6.44	2.41	0.37	0.90	2.27	0.64
(e)	10	1.38	4.46	2.03	0.46	0.92	2.39	0.87
(f)	3	0.81	2.80	1.64	0.59	0.96	2.59	1.22

2. CAV$_{02}$

FIG. 10. Transmission spectra vs the rf frequency and the **H** field. Fitted polariton branches are shown in white. The BM frequency (in orange) and the coupling strength are variables. The FMR is shown in black and the DM in red. Fitted parameters are shown in Table III.

TABLE III. The parameters associated with measurements at different values of distance d between the post and the lid of the printed cavity. The numbering refers to the spectra shown in Fig. 10.

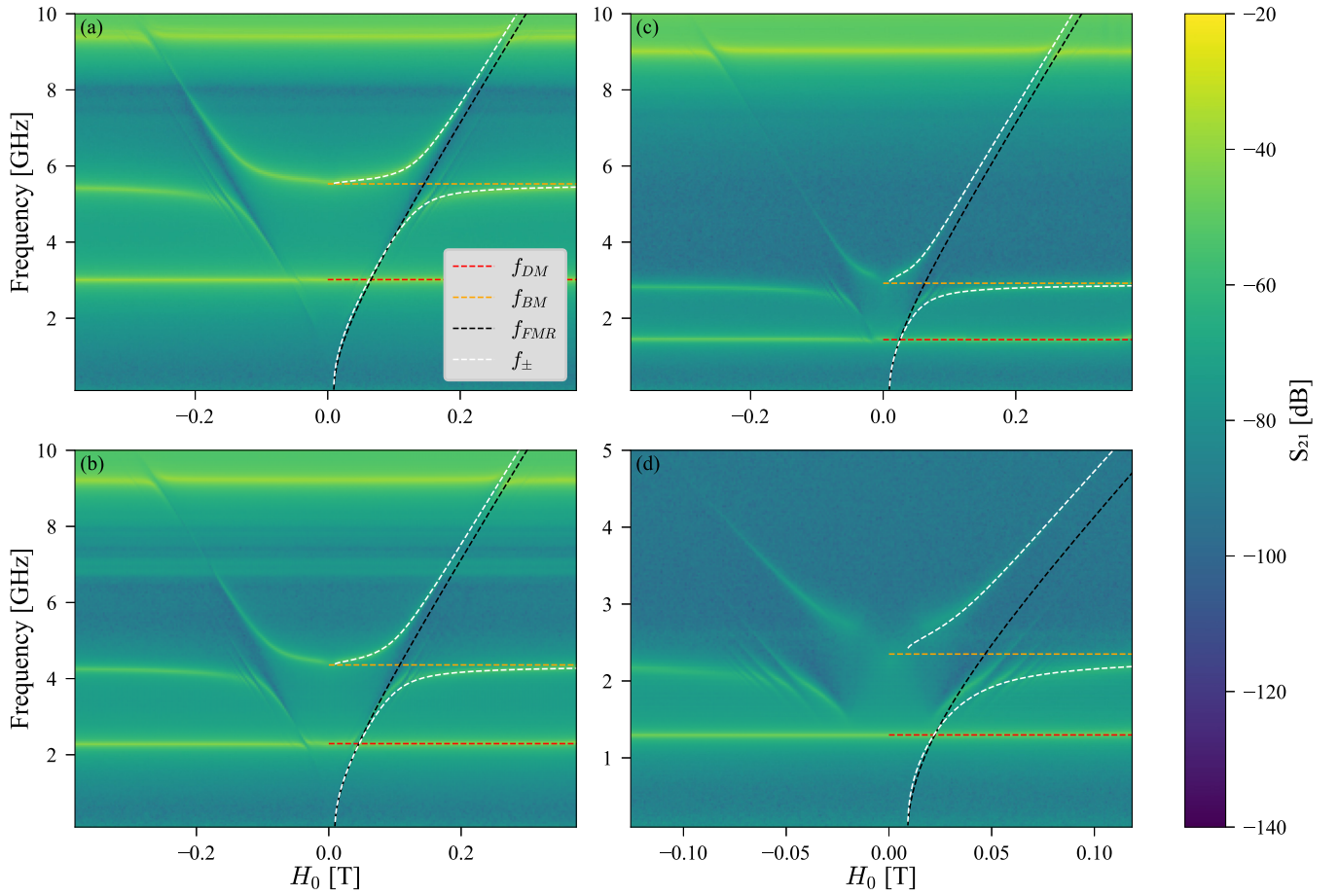| Numbering	f_{DM} [GHz]	f_{BM} [GHz]	$g/2\pi$ [GHz]	g/ω	$g^2/2\pi\omega$ [GHz]	$\Delta_m/2\pi$ [GHz]	f_{gap} [GHz]
(a)	4.06	9.79	2.72	0.28	0.76	1.63	0.24
(b)	3.26	8.76	2.59	0.30	0.77	1.71	0.30
(c)	3.01	8.32	2.52	0.30	0.76	1.74	0.31
(d)	2.64	7.63	2.42	0.32	0.77	1.69	0.34

3. CAV$_{03}$

FIG. 11. Transmission spectra vs the rf frequency and the **H** field. Fitted polariton branches are shown in white. The BM frequency (in orange) and the coupling strength are variables. The FMR is shown in black and the DM in red. Fitted parameters are shown in Table IV.

TABLE IV. The parameters associated with measurements at different values of distance d between the post and the lid of the cavity with cylinder posts from [29]. The numbering refers to the spectra shown in Fig. 11.

Numbering	f_{DM} [GHz]	f_{BM} [GHz]	$g/2\pi$ [GHz]	g/ω	$g^2/2\pi\omega$ [GHz]	$\Delta_m/2\pi$ [GHz]	f_{gap} [GHz]
(a)	3.02	5.53	0.65	0.12	0.08	0.33	0.01
(b)	2.29	4.36	0.69	0.16	0.11	0.29	0.02
(c)	1.44	2.92	0.63	0.22	0.14	0.37	0.02
(d)	1.30	2.35	0.58	0.25	0.14	0.50	0.05
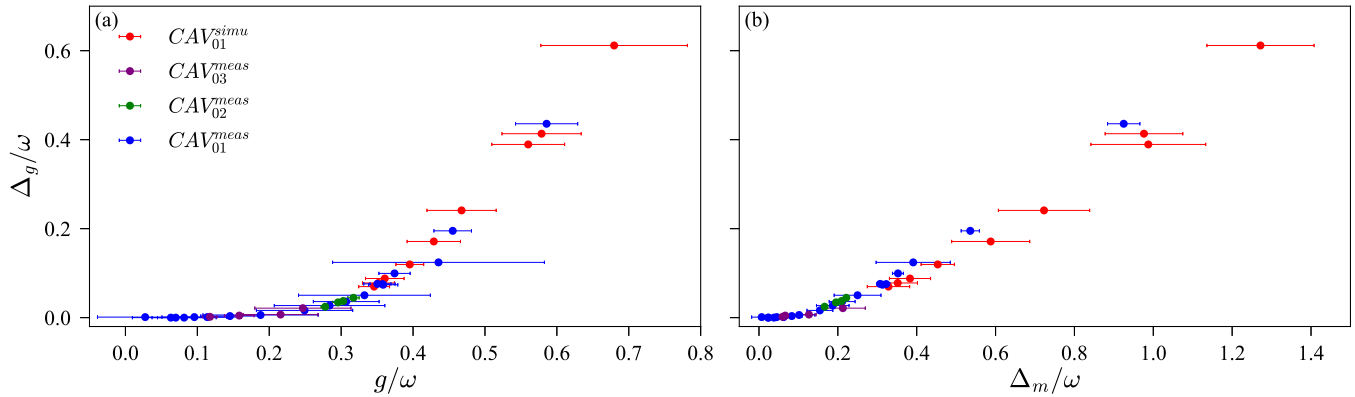
FIG. 12. Δ_g/ω vs (a) g/ω; (b) Δ_m/ω. Shown are the FD simulations on CAV_{01} in red and measurements in blue, in green for CAV_{02}, and in purple for CAV_{03}.

APPENDIX G: GAP STUDY

Without adding Δ_m to the FMR in the Dicke model, and without applied static magnetic field, the frequency of the upper polariton is equal to the cavity one. However, when the FMR is shifted, an observable forbidden gap in frequency appears. Considering Fig. 12, Δ_g/ω is not observable when g/ω is equal to or lower than 0.2. For higher g/ω values, Δ_g/ω is quadratic, as shown in (a). In (b) is shown the evolution of Δ_g/ω versus Δ_m/ω.

[1] Ö. O. Soykal and M. E. Flatté, Strong Field Interactions between a Nanomagnet and a Photonic Cavity, Phys. Rev. Lett. **104**, 077202 (2010).

[2] H. Huebl, C. W. Zollitsch, J. Lotze, F. Hocke, M. Greifenstein, A. Marx, R. Gross, and S. T. B. Goennenwein, High Cooperativity in Coupled Microwave Resonator Ferrimagnetic Insulator Hybrids, Phys. Rev. Lett. **111**, 127003 (2013).

[3] Y. Tabuchi, S. Ishino, T. Ishikawa, R. Yamazaki, K. Usami, and Y. Nakamura, Hybridizing Ferromagnetic Magnons and Microwave Photons in the Quantum Limit, Phys. Rev. Lett. **113**, 083603 (2014).

[4] L. Bai, M. Harder, Y. P. Chen, X. Fan, J. Q. Xiao, and C.-M. Hu, Spin Pumping in Electrodynamically Coupled Magnon-Photon Systems, Phys. Rev. Lett. **114**, 227201 (2015).

[5] M. Harder, B. M. Yao, Y. S. Gui, and C.-M. Hu, Coherent and dissipative cavity magnonics, J. Appl. Phys. **129**, 201101 (2021).

[6] D. Lachance-Quirion, Y. Tabuchi, A. Gloppe, K. Usami, and Y. Nakamura, Hybrid quantum systems based on magnonics, Appl. Phys. Express **12**, 070101 (2019).

[7] B. Z. Rameshti, S. V. Kusminskiy, J. A. Haigh, K. Usami, D. Lachance-Quirion, Y. Nakamura, C.-M. Hu, H. X. Tang, G. E. W. Bauer, and Y. M. Blanter, Cavity magnonics, Phys. Rep. **979**, 1 (2022).

[8] A. J. B. Fuller, *Ferrites at Microwave Frequencies*, IEE Electromagnetic Waves Series, Vol. 23 (Peter Peregrinus, Ltd., London, 1987), p. 277.

[9] X. Zhang, C.-L. Zou, N. Zhu, F. Marquardt, L. Jiang, and H. X. Tang, Magnon dark modes and gradient memory, Nat. Commun. **6**, 8914 (2015).

[10] J. Bourhill, W. Yu, V. Vlaminck, G. E. W. Bauer, G. Ruoso, and V. Castel, Generation of Circulating Cavity Magnon Polaritons, Phys. Rev. Appl. **19**, 014030 (2023).

[11] W. Yu, T. Yu, and G. E. W. Bauer, Circulating cavity magnon polaritons, Phys. Rev. B **102**, 064416 (2020).

[12] C. Ciuti, G. Bastard, and I. Carusotto, Quantum vacuum properties of the intersubband cavity polariton field, Phys. Rev. B **72**, 115303 (2005).

[13] A. A. Anappara, S. De Liberato, A. Tredicucci, C. Ciuti, G. Biasiol, L. Sorba, and F. Beltram, Signatures of the ultrastrong light-matter coupling regime, Phys. Rev. B **79**, 201303(R) (2009).

[14] A. F. Kockum, A. Miranowicz, S. De Liberato, S. Savasta, and F. Nori, Ultrastrong coupling between light and matter, Nat. Rev. Phys. **1**, 19 (2019).

[15] P. Forn-Díaz, L. Lamata, E. Rico, J. Kono, and E. Solano, Ultrastrong coupling regimes of light-matter interaction, Rev. Mod. Phys. **91**, 025005 (2019).

[16] F. Yoshihara, T. Fuse, Z. Ao, S. Ashhab, K. Kakuyanagi, S. Saito, T. Aoki, K. Koshino, and K. Semba, Inversion of Qubit Energy Levels in Qubit-Oscillator Circuits in the Deep-Strong-Coupling Regime, Phys. Rev. Lett. **120**, 183601 (2018).

[17] J. Keller, G. Scalari, F. Appugliese, S. Rajabali, M. Beck, J. Haase, C. A. Lehner, W. Wegscheider, M. Failla, M. Myronov, D. R. Leadley, J. Lloyd-Hughes, P. Nataf, and J. Faist, Landau polaritons in highly nonparabolic two-dimensional gases in the ultrastrong coupling regime, Phys. Rev. B **101**, 075301 (2020).

[18] F. Benz, M. K. Schmidt, A. Dreismann, R. Chikkaraddy, Y. Zhang, A. Demetriadou, C. Carnegie, H. Ohadi, B. de Nijs, R. Esteban, J. Aizpurua, and J. J. Baumberg, Single-molecule optomechanics in "picocavities," Science **354**, 726 (2016).

[19] M. Goryachev, W. G. Farr, D. L. Creedon, Y. Fan, M. Kostylev, and M. E. Tobar, High-Cooperativity Cavity QED with Magnons at Microwave Frequencies, Phys. Rev. Appl. **2**, 054002 (2014).

[20] J. Bourhill, N. Kostylev, M. Goryachev, D. L. Creedon, and M. E. Tobar, Ultrahigh cooperativity interactions between magnons and resonant photons in a YIG sphere, Phys. Rev. B **93**, 144420 (2016).

[21] G. Flower, M. Goryachev, J. Bourhill, and M. E. Tobar, Experimental implementations of cavity-magnon systems: From ultra strong coupling to applications in precision measurement, New J. Phys. **21**, 095004 (2019).

[22] I. A. Golovchanskiy, N. N. Abramov, V. S. Stolyarov, A. A. Golubov, M. Yu. Kupriyanov, V. V. Ryazanov, and A. V. Ustinov, Approaching Deep-Strong On-Chip Photon-to-Magnon Coupling, Phys. Rev. Appl. **16**, 034029 (2021).

[23] I. A. Golovchanskiy, N. N. Abramov, V. S. Stolyarov, M. Weides, V. V. Ryazanov, A. A. Golubov, A. V. Ustinov, and M. Y. Kupriyanov, Ultrastrong photon-to-magnon coupling in multilayered heterostructures involving superconducting coherence via ferromagnetic layers, Sci. Adv. **7**, eabe8638 (2021).

[24] X. Zhang, C.-L. Zou, L. Jiang, and H. X. Tang, Strongly Coupled Magnons and Cavity Microwave Photons, Phys. Rev. Lett. **113**, 156401 (2014).

[25] C. Zhang, Y. Shi, W. Zhang, C. Jiang, and G. Chai, Ultra-strong magnon-photon coupling induced in the photonic crystals with an YGaGeIG defect, Appl. Phys. Lett. **115**, 022407 (2019).

[26] Y. Cao, P. Yan, H. Huebl, S. T. B. Goennenwein, and G. E. W. Bauer, Exchange magnon-polaritons in microwave cavities, Phys. Rev. B **91**, 094423 (2015).

[27] B. Z. Rameshti, Y. Cao, and G. E. W. Bauer, Magnetic spheres in microwave cavities, Phys. Rev. B **91**, 214430 (2015).

[28] R. H. Dicke, Coherence in spontaneous radiation processes, Phys. Rev. **93**, 99 (1954).

[29] J. Bourhill, V. Castel, A. Manchec, and G. Cochet, Universal characterization of cavity–magnon polariton coupling strength verified in modifiable microwave cavity, J. Appl. Phys. **128**, 073904 (2020).

[30] C. Kittel, On the theory of ferromagnetic resonance absorption, Phys. Rev. **73**, 155 (1948).

[31] R. I. Joseph and E. Schlömann, Demagnetizing field in nonellipsoidal bodies, J. Appl. Phys. **36**, 1579 (1965).

[32] T. Niemczyk, F. Deppe, H. Huebl, E. P. Menzel, F. Hocke, M. J. Schwarz, J. J. Garcia-Ripoll, D. Zueco, T. Hümmer, E. Solano, A. Marx, and R. Gross, Circuit quantum electrodynamics in the ultrastrong-coupling regime, Nat. Phys. **6**, 772 (2010).

[33] J. J. Hopfield, Theory of the contribution of excitons to the complex dielectric constant of crystals, Phys. Rev. **112**, 1555 (1958).

[34] A. F. Kockum, A. Miranowicz, V. Macrì, Salvatore Savasta, and F. Nori, Deterministic quantum nonlinear optics with single atoms and virtual photons, Phys. Rev. A **95**, 063849 (2017).

[35] L. Garziano, R. Stassi, V. Macrì, A. F. Kockum, S. Savasta, and F. Nori, Multiphoton quantum Rabi oscillations in ultrastrong cavity QED, Phys. Rev. A **92**, 063830 (2015).

[36] Z.-B. Yang, H. Jin, J.-W. Jin, J.-Y. Liu, H.-Y. Liu, and R.-C. Yang, Bistability of squeezing and entanglement in cavity magnonics, Phys. Rev. Res. **3**, 023126 (2021).

[37] M. X. Bi, C. J. Dai, J.-L. Che, M.-L. Hu, and X. H. Yan, Bistability of cavity magnon polaritons beyond the Holstein–Primakoff transformation, J. Appl. Phys. **130**, 243902 (2021).

[38] Z.-B. Yang, W.-J. Wu, J. Li, Y.-P. Wang, and J. Q. You, Steady-entangled-state generation via the cross-Kerr effect in a ferrimagnetic crystal, Phys. Rev. A **106**, 012419 (2022).

[39] W.-J. Wu, D. Xu, J. Qian, J. Li, Y.-P. Wang, and J.-Q. You, Observation of nonlinearity and heating-induced frequency shifts in cavity magnonics, Chinese Phys. B **31**, 127503 (2022).

[40] G. Zhang, Y. Wang, and J. You, Theory of the magnon Kerr effect in cavity magnonics, Sci. China Phys. Mech. Astron. **62**, 987511 (2019).

[41] F. Rana, Quantum optics lectures ECE5310, Cornell University, https://courses.cit.cornell.edu/ece531/Lectures/chapter5.pdf.

[42] A. Prabhakar and D. D. Stancil, *Spin Waves, Theory and Applications* (Springer, New York, NY, 2009).

[43] K. Hepp and E. H. Lieb, On the superradiant phase transition for molecules in a quantized radiation field: The Dicke maser model, Ann. Phys. **76**, 360 (1973).